Lenticular Ga-oxide nanostructures in thin amorphous germanosilicate layers - Size control and dimensional constraints

Jacopo Remondina [a], Silvia Trabattoni [a], Adele Sassella [a], Nikita V. Golubev [c], Elena S. Ignat'eva [c], Vladimir N. Sigaev [c], Maurizio Acciarri [a], Benedikt Schrode [b], Roland Resel [b], Alberto Paleari [a,c,*], Roberto Lorenzi [a]

[a] Department of Materials Science, University of Milano-Bicocca, Via R. Cozzi 55, I-20125 Milano, Italy
[b] Institute of Solid-State Physics, Graz University of Technology, Petersgasse 16, AU-8010 Graz, Austria
[c] P. Sarkisov International Laboratory of Glass-based Functional Materials, Mendeleev University of Chemical Technology of Russia, Miusskaya Square 9, 125047 Moscow, Russia

HIGHLIGHTS

- Ga-oxide nanophases in films are directly obtained from glass target by sputtering.
- Ga-oxide in silicate films unveils a hierarchical architecture of nanoaggregation.
- Nano-segregation of Ga-oxide in silicate films occurs even in films few nm thick.
- Ga-oxide nanosize in oxide films can be controlled by treatments and thickness.
- Sputtering and treatments enable the use of Ga-oxide nanophases in planar geometry.

GRAPHICAL ABSTRACT
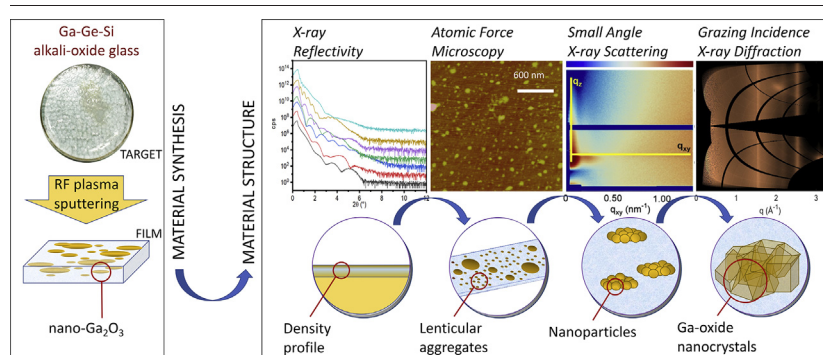
ARTICLE INFO

ABSTRACT

Gallium incorporation in silicate glasses gives rise to compounds in which the nucleation and growth of Ga-oxide nanostructures can be designer controlled so as to obtain a number of functional properties for photonic applications. However, despite planar geometry pertains to a large part of modern technology, no information is available yet on the scalability of Ga-oxide segregation mechanisms in oxide thin films. In fact, incorporated Ga-oxide nanostructures have only been obtained in bulk materials. Here we show that deposition of Ga-alkali-germanosilicate thin films by radiofrequency-plasma sputtering gives rise to Ga-oxide nanostructures incorporated in an amorphous matrix. X-ray diffraction, X-ray reflectivity, small-angle X-ray scattering, and atomic force microscopy data unveil the formation of lenticular nanoaggregates, only a few nm thick, even in as-deposited materials as a result of two-dimensional aggregation of spinel-like Ga_2O_3 nanoparticles. Importantly, the aggregate size distribution is controlled not only by the temperature but also by the film thickness when it is reduced from 10^2 nm to only a few nm. The results open the way to the design of oxide-in-oxide thin films with incorporated networks of nanostructures which can act as percolation paths for unconventional electric responses in neuromorphic functional systems.

* Corresponding author at: Department of Materials Science, University of Milano-Bicocca, Via R. Cozzi 55, I-20125 Milano, Italy.
E-mail address: alberto.paleari@unimib.it (A. Paleari).

1. Introduction

Composition and nano-inhomogeneity are the main factors which determine the propensity of an amorphous mixed oxide to undergo phase separation [1]. Such a propensity is crucial to obtain nanostructured glass-based materials in which nanophases can be induced and controlled so as to be the source of specific functional features [2]. Important cases regard the design of nanostructured oxide systems with wide-band-gap nano-particles [3]. In these systems, the nanophase can provide the resulting material with technologically important properties in the fields of optics and photonics, preserving chemical stability and workability of the starting amorphous matrix [4–7]. For this reason, during the last years, different groups have analysed how nanostructured functional glasses can be obtained in bulk material by phase separation of oxide-in-oxide phases [3,6,8,9]. In this field, a number of studies have recently concerned Ga-containing mixed oxides. These works have demonstrated that Ga_2O_3 nanoparticles with controlled size, from 10^0 to about 10^1 nm [10,11], can represent a breakthrough in various applications [12,13]. In fact, Ga_2O_3 containing glasses can take advantage of either intrinsic nanophase features, or light-emission properties of ions hosted by the nanophase [12–19].

However, despite the technological potential of nanostructured oxides in 2D-planar geometry – especially in optoelectronics and light-emitting devices – the amount of data on the scalability of glass nanostructuring propensity of wide-band-gap oxide-in-oxide systems in planar geometry is not large and is mainly focused on quantum dots containing films [20,21]. There are only a few works on oxide films with incorporated oxide nanophases [6,9,22], and a recent study on charge transport properties of Ga-oxide containing films [23]. In this regard, it is worth noting that dielectric oxide thin films can potentially give rise to unconventional electric transport properties with responsive features. For instance, electric field switchable conductive paths can occur in oxide layers by defect-mediated or charge trapping processes [24–29], or by conductive bridging through nanostructure forming/dissolving or inhibiting mechanisms [30–32]. This kind of systems can potentially open new perspectives in the design of integrated units for neuromorphic networks of information processing and storage, mainly for Big Data applications [33]. The design of nanostructured features suitable for charge transport are also relevant for the exploitation of electrically driven photonic properties for light-emitting-devices, where wide-band-gap materials have a role as blue-UV emitters. However, in the case of Ga-containing oxides, detailed information on Ga-oxide nanophases in oxide films is apparently lacking. Specifically, no data are available on the need and role of thermal activation in the formation of Ga-oxide phases in amorphous oxide layers and, importantly, on the possible effects of spatial constraints from reduced-thickness on the phase separation process.

Aim of the present work is to provide an experimental basis about the 2D-scalability of the process of Ga-oxide nanostructure formation in glass matrixes, so as to enable the implementation of this class of nanostructures in thin oxide films. Along this line, the present work intends to give first experimental evidence and structural interpretation of the process of nanostructuring in thin layers of Ga-containing amorphous matrixes of alkali-germanosilicate, at thickness comparable with the nanoparticle size. The collected results are also aimed at obtaining information on the real role of thickness and thermal post-synthesis treatments on size and amount of segregated Ga-oxide, in the perspective of a future design and control of fabrication processes of Ga-oxide containing glass-based devices in planar geometry, specifically for optoelectronics and for responsive devices for neuromorphic computing networks.

2. Experimental approach and methods

The experimental results of the present study are articulated into four kinds of outcomes which concur together to give a picture of the
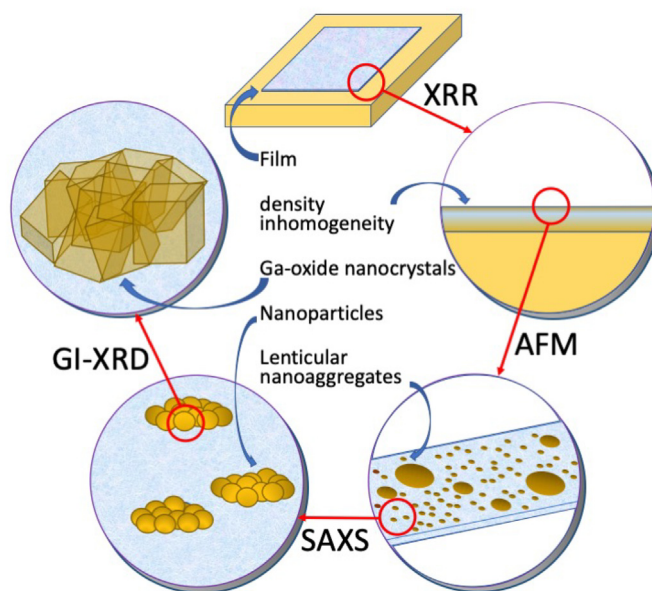

Fig. 1. Rationale of the investigation. In-plane and out-of-plane nanostructured features emerge on the different structural scales from an articulated complex of experimental techniques: X-ray reflectivity (XRR), atomic force microscopy (AFM), small angle X-ray scattering (SAXS), and grazing incidence X-ray diffraction (GI-XRD). The analysis finally gives a view of the lenticular nano-aggregation and the nearly isotropic nanophase crystallization.

nanostructured oxide-in-oxide system and the involved mechanisms of its formation on the different length scales (Fig. 1). X-ray reflectivity (XRR) data and profilometry give information on mean film density, thickness, and electronic density profile with respect to the bulk glass; atomic force microscopy (AFM) give images of the in-plane sub-micrometre morphology of the oxide thin films; small angle X-ray scattering (SAXS) data – collected both in-plane and out-of-plane – is used to evaluate the mean nanostructure anisotropy; finally, X-ray diffraction (XRD) patterns identify the crystal phase of the nanostructures and, importantly, the in-plane and out-of-plane domain of crystallinity to be compared with the nanoparticle morphology.

The structural analysis just outlined is applied to a matrix of samples comprising as-deposited films with different thickness, films at fixed thickness after post-synthesis treatments at different temperatures in the range where nucleation is observed in bulk, and films with different thickness after treatment at a fixed temperature close to the crystallization temperature of bulk material. Finally the information is elaborated so as to give a picture of the mechanisms driving the native formation of nanostructures and their thermally activated growth.

2.1. Materials and sample preparation

The investigated films were produced by radiofrequency-plasma (RF) sputtering from a glass target 6 cm in diameter and 5 mm thick. The glass target with nominal composition of $7.5Li_2O$-$2.5Na_2O$-$20Ga_2O_3$-$45GeO_2$-$25SiO_2$ mol% was prepared using amorphous SiO_2 (special purity grade), GeO_2 (special grade), Li_2CO_3 (reagent grade), Na_2CO_3 (reagent grade), and Ga_2O_3 (reagent grade). The amounts of starting materials – from a few g to tens of g, depending on the stoichiometric coefficients – were weighed using an analytical balance with an accuracy of 0.001 g and carefully mixed in an agate mortar. The batch was melted in an uncovered Pt crucible in an electrically heated furnace at 1500 °C for 60 min. The melt was cast into an unheated steel mould.

The film deposition on oxidized silicon substrates by RF sputtering was performed by means of a homemade instrument comprising a radiofrequency generator, working at 13.56 MHz and 250 W, a deposition chamber made of steel, and a substrate holder consisting of a copper

plate. The distance between target and substrate was about 15 cm. Internal pressure and gas flow were obtained and controlled by rotary and turbo-molecular pumps. During the sputtering, a dynamic equilibrium was maintained in which Ar gas carrier was fluxed into the sputtering chamber at about 1.6 standard cubic cm per min and pumped out by turbo-molecular pump. The flow conditions resulted in a working pressure of 6.0×10^{-3} mbar. To avoid contaminations from the air (especially from nitrogen and carbon dioxide), the chamber was previously vacuumed down to a pressure of $3–5 \times 10^{-5}$ mbar several times and purging with Ar. Machine testing with an Al reference target did not show detectable contamination. The experimental procedure and the specific sputtering conditions were optimized designing the process so as to obtain films with thickness spanning two orders of magnitude – from few nm to more than 100 nm – in a single deposition run. Carrier gas pressure and voltage were adjusted so as to limit the deposition time within 1 h keeping the voltage fixed at about the maximum value of 1.1 kV. Within these constraints, the process optimization demonstrated to assure a constant deposition rate in the whole range of deposition duration, from 1 h down to a fraction of min. The sputtering conditions so optimized were kept fixed in the entire set of deposition runs, so as to extract reliable data on the possible effects of the investigated parameters – thickness and treatment – on the material features. Changes of the sputtering conditions could in fact determine relevant modifications of the material features and of the underlying evolution resulting from thermal treatments, as reported since the early works on RF sputtering technique [34,35] and in recent works on nanostructured materials [36,37].

This system was used to deposit up to 4 films at a time with an area of about 2×2 cm^2 and without relevant inhomogeneity within a single film. After deposition, some of the films were thermally treated in a furnace for 30 min at 700 °C with hot insertion and removal. Other films were thermally treated for different duration (from 1 min to 2 h) or at lower temperature (down to 600 °C). Finally, a matrix of film samples was obtained with thickness ranging between about 1 to 130 nm, comprising as-deposited and thermally treated films at different treatment temperature and durations.

2.2. Experimental techniques

The film thickness was measured by means of a stylus profilometer (Veeco Dektak 8) with a sensitivity of 0.8 nm. Thickness measurements were obtained by collecting height profiles across a step between the surface of the deposited film and the substrate surface preserved during the sputtering process by a polyimide film then removed. Mean thickness value and uncertainty were estimated on 6 profile measurements on each sample along different directions. A final standard deviation of about 20 nm was obtained, enough for estimating the deposition rate with a final uncertainty of about 1 nm/min through a set of measurements at sputtering time ranging more than two orders of magnitude.

X-ray reflectivity and specular X-ray diffraction experiments were performed with an PANalytical Empyrean equipment using a copper anode and a multilayer mirror as monochromator ($\lambda = 1.542$ Å) and a PIXcel3D detector operating in 1D mode (diffraction measurements) or in 0D mode (for reflectivity measurements). XRD measurements were collected from 8° to 80° (2θ) for an acquisition time of about 15 h, while XRR from 0° to 6° (ω) with a total acquisition time of 2 h. Electron density profiles were calculated from the reflectivity curves by using the software StochFit [38].

GI-XRD experiments at grazing incidence were carried out using synchrotron light at the beamline XRD1 at Elettra (Trieste, Italy). The experiments were carried out with monochromatic radiation at $\lambda = 1.4$ Å and a Dectris Pilatus 2 M detector placed from 150 to 200 mm from the sample centre. Data were collected at various grazing incidence angles, obtaining the best definition at $\omega = 0.5°$. Transfer of the data into reciprocal space and subsequent data evaluation was

performed by the software GIDVis [39]. The width of the peaks was used to determine the size of the crystals by using the Scherrer formula $D = l/[D(2\theta)\cos(\theta)]$ where $D(2\theta)$ is the peak full width at half maximum. The XRD intensity of the crystalline phase was analysed as a function of material parameters evaluating the net area of the main reflection of the crystalline phase after normalization for the acquisition time.

SAXS investigations were performed at the SAXS beamline at the synchrotron Elettra using a wavelength of 1.55 Å with a Dectris Pilatus 1 M detector at 2 m from the sample centre.

AFM images were collected using a Bruker MultiMode Nanoscope V in intermittent-contact mode in air with Si tips (frequency 340 kHz, spring constant 40 N/m, tip radius 8 nm).

3. Results and discussion

3.1. Film thickness and density profile at the nanoscale

Film thickness is an important parameter of the present study, representing a potential constraint to the nanostructuring process. Thickness reduction, down to values of only a few nm, could indeed affect size and number of the nanostructures. For this reason, the inspection of our oxide-in-oxide system on the different length scales starts by exposing thickness data from profilometry measurements and XRR patterns.

Fig. 2a reports the profilometric values of film thickness *vs.* deposition time, which follow a linear relationship corresponding to a deposition rate of about 2 nm/min. Fig. 2b shows the results of a comparison between thickness data collected before (circles) and after (squares) thermal treatments, at temperature ranging between 600 and 700 °C, within a set of samples with thickness of 140 ± 20 nm. Importantly, the data do not show any relevant change after treatment. This outcome, despite its simplicity, gives a first indication about the density of as-deposited material. In fact, since the thickness does not change – even if the treatment temperature is higher than the glass transition in bulk material and close to its nano-crystallization temperature [40] – the data suggest a density value probably similar to the density of the glass target.

Confirmation that the film density is congruent with that of bulk material can be found by analysing the XRR patterns of the investigated films. Fig. 2c and d – which reports, respectively, XRR data collected on as-deposited and thermally treated films – display typical XRR features consisting in a periodically modulated angular dependence of the reflected intensity, superimposed to an overall signal attenuation [41]. These features, analogously to the optical intensity modulation from interference effects of reflected light from thin transparent layers, contain information on thickness and electronic density of the analysed film [42,43]. The spacing of the modulation mainly depends on thickness, while the electronic density determines the critical angle of total reflection above which the modulated signal decreases. The decreasing behaviour at increasing angle is instead mainly influenced by the film surface roughness.

Starting from XRR data (and using the electron density of the oxidized Si substrate as a reference), the electronic density can be calculated and compared with the value expected from the nominal composition. Fig. 2e and f report the electronic density profiles and the film thickness calculated by fitting the XRR patterns according to Parratt-derived models [38].

It is worth noting that the calculated thickness agrees with the values independently obtained by profilometry (Fig. 2a), at least within the uncertainty of the model and the experimental reproducibility of film thickness. Anyway, the analysis confirms that the XRR patterns and the calculated density profiles appear scarcely modified by the thermal treatment. Furthermore, the average value in the density profiles matches quite well the expected electronic density of the nominal composition calculated from the mass density values of the parent oxides, as
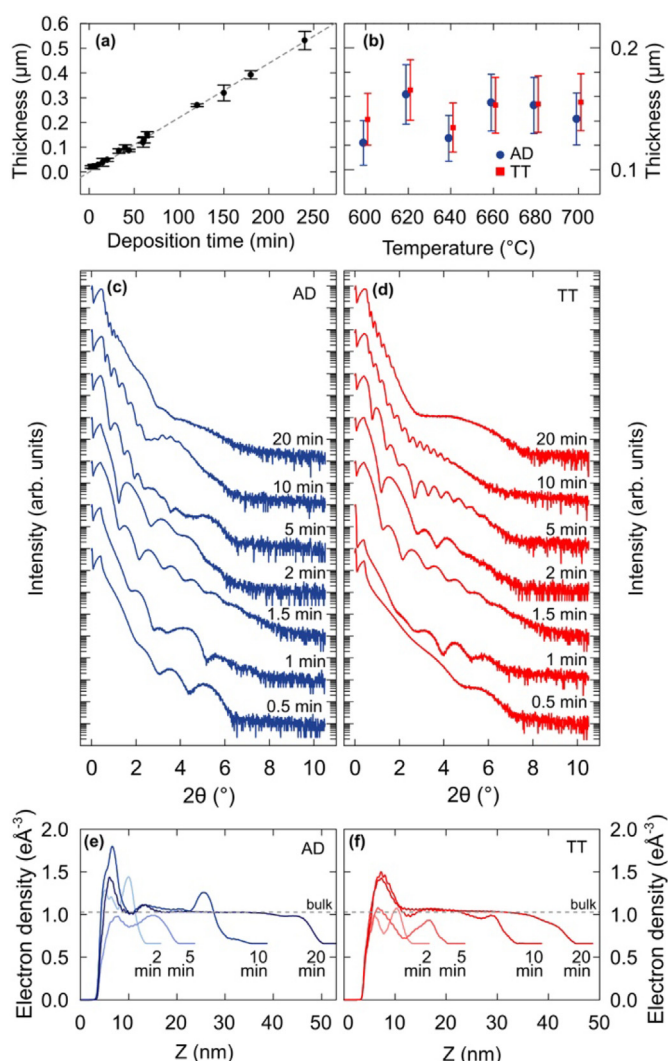
Fig. 2. Profilometry and X-Ray Reflectivity data. (a) Thickness of as-deposited film *vs.* deposition time collected by profilometry technique. The straight line is the linear fit of the data with a slope of 2.15 ± 0.03 nm/min. (b) Comparison between thickness values measured on a set of films with comparable thickness, as-deposited (circles) and after (squares) thermal treatment at the indicated temperature for 30 min. (c) and (d) XRR patterns of films before and, respectively, after thermal treatment at 700 °C for 30 min; film deposition time are indicated. (e) and (f) Electron density profiles along the *Z*-axis normal to the film surface, as calculated from XRR patterns of thicker films in (c) and (d), according to Parratt-derived models and using the SiO_2 substrate electron density $(0.67 \, e\text{Å}^{-3})$ as an internal reference; grey lines are drawn as a reference of the bulk value calculated from the nominal composition.

reported for comparison in Fig. 2e and f. In other words, as-deposited and thermally treated films possess a density congruent with a fully densified composition which reproduce the mean structure of the parent bulk glass.

Secondary structures in the calculated density profiles (appearing as density peaks in Fig. 2e and f at the top layer of the film mainly, but also at the interphase with the substrate) suggest some structural inhomogeneity. This data, despite the large uncertainty of the quite indirect calculation, points to some kind of phase separation and constitutes a preliminary evidence of nanostructures across the film thickness.

3.2. In-plane nanostructure morphology and size

In the present system, as already reported in analogous phase-separated materials [23], the analysis of the morphology of the film surface can distinctly signal the occurrence of nanostructures and confirm

the preliminary XRR indication of nano-inhomogeneity. The AFM images in Fig. 3 indeed register clear-cut nanostructures, with a dependence on thermal treatment (Fig. 3a–c; Fig. 3d reports the resulting nanostructure number density in the indicated size ranges) and on thickness (Fig. 3e–g; Fig. 3h reports the resulting nanostructure number density in the same size ranges indicated in Fig. 3d). Importantly, nearly circular nanostructures are distributed on the film surface not only in thermal treated but in as-deposited material too. The main effect of thermal treatments is the enhanced mean size of the nanostructures.

Actually, the images show three quite distinct nanoparticle populations with clearly different size. A few large nanostructures (just below 1 μm in lateral size) are found together with a relatively larger abundance of just smaller nanostructures (about 10^2 nm in lateral size), all dispersed among a relatively larger number of significantly smaller nanostructures (with a quite narrow size distribution at around values of the order of 10^1 nm). Comparing AFM images before and after treatment at two temperatures (Fig. 3a–c), clear changes are registered in the number of nanostructures belonging to the three populations.

The quantitative analysis of the size distribution in Fig. 3d shows that the number of small nanoparticles per unit area grows from as-deposited sample to sample treated at 640 °C, and decreases when the treatment temperature is increased up to 700 °C. The population of nanoparticles with intermediate size – which is approximately equal in number to the small nanoparticles before treatment – instead decreases after treatment. Few greater nanostructures are also observed, whose number is enhanced by the thermal treatment and increases with the treatment temperature. These features are expected in a mechanism of thermally activated nucleation of nanoparticles from phase separation and nanoparticle aggregation [10,14]. In fact, the decrease of the number of small nanoparticles per unit area when the treatment temperature is enhanced up to 700 °C is just the expected behaviour if the nucleation process ceases to be so efficient to dominate the processes of formation and growth of large nanostructures by aggregation between small nanoparticles and by ripening mechanisms. In this regard, the investigated films display features qualitatively similar to what observed in bulk material – despite the different propensity to form native nanostructures – in which the nucleation efficiency has a maximum at temperatures close to the glass transition.

Since all these kinds of processes are mediated by diffusion mechanisms, dimensional constraints can in principle influence the nanostructures – analogously to aggregates and clusters arising from two-dimensionally constrained multicomponent systems [44–46] – as a result of the reduction of thickness below the scale of the nanostructure size. Data on this point can be extracted from the AFM images in Fig. 3e–g on as-deposited films of different thickness. The size distribution analysis in Fig. 3h – obtained by filtering the nanostructure count according to the same three size populations in the analysis of thermal treatment effects – shows an initial increase of small and medium size nanoparticles by increasing the film thickness from 1 to a few nm. When the thickness becomes larger than 10^2 nm, there is a further increase of medium nanoparticles accompanied by the formation of big aggregates and a reduction of the number of small nanoparticles. These data suggest that the process of coalescence of nanoparticles in larger aggregates is favoured in thicker films and eventually prevails on nanoparticle nucleation. This fact can partially be ascribed to the deposition time, which promotes larger phase separation and aggregation in thicker than in thin films during the deposition process. Nevertheless, the planar geometry can contribute to this effect by hindering the process of nanoparticle aggregation into larger nanostructures. In fact, the AFM survey of in-plane nanostructure morphology indirectly highlights an evident effect of planar geometry on the mechanism of phase separation. The in-plane size of the observed nanostructures – in all the analysed films, no matter how much the size distribution is modified by treatments – turns out to be much larger, in average, than the film thickness: from several tens of nm in films a few nm thick (Fig. 3f), up to about 1 μm in all other films (as in Fig. 3c, g), whose thickness does
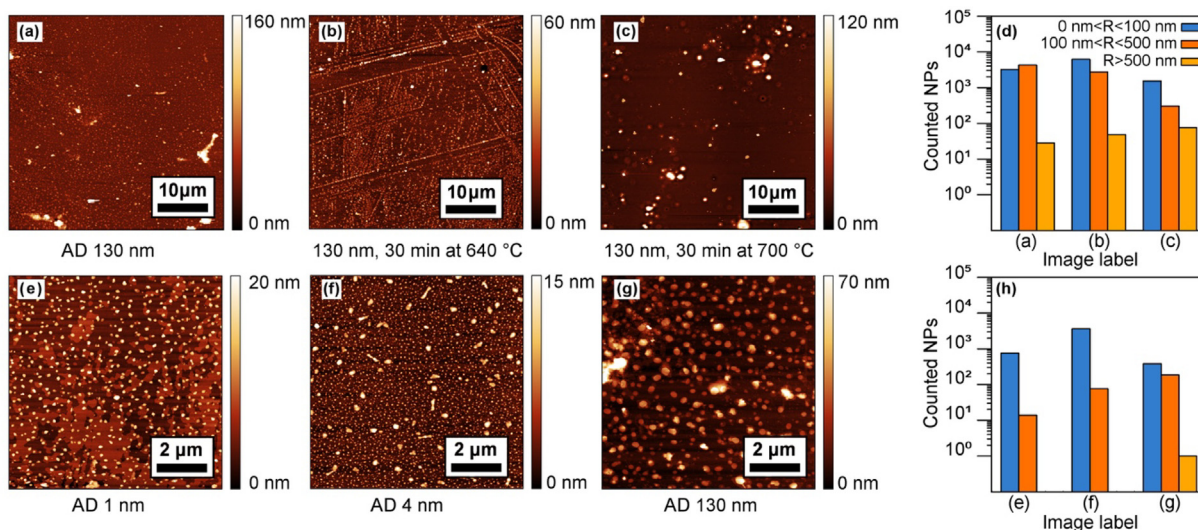
Fig. 3. Atomic Force Microscopy analysis. (a), (b) and (c) AFM images of films with equal thickness (about 130 nm) as-deposited (AD) and after thermal treatment at the indicated time and temperature conditions. (d) Bar plot of the number of nanoparticles (NPs) counted in the AFM images (a)-(c) and grouped in three populations according to the lateral size. (e), (f) and (g) AFM images of as-deposited films with different thickness, as indicated (image in (g) is collected in the central region of the area analysed in (a)). (h) Bar plot of the number of NPs counted in the AFM images (e)-(g) and grouped in three populations according to the lateral size.

not exceed 130 nm. Therefore, this outcome points to lenticular nanostructures. Such a morphology is indeed unprecedented in this kind of material in bulk, which previously shows to form basically spherical nanostructures [3,8,9,11–13,15–17].

3.3. Nanostructure surface and shape anisotropy

Further information on the nanostructure morphology can be obtained from the analysis of SAXS patterns collected in the full angular field of scattering at grazing incident angle both on an as-deposited film and on a bulk nanostructured sample (Fig. 4a, b, respectively). The full analysis of this kind of data by means of a single scattering function requires complex simulation models [47], which can hardly be efficiently applied in the investigated films, where homogeneity and isotropy of nanostructure distribution and aggregation cannot be assumed. Nevertheless, from the data in Fig. 4a, simpler SAXS patterns can be extracted so as to perform a semi-quantitative analysis of the scattering data in terms of structural levels of the system [47,48], especially with the help of AFM results and the comparison with the nanostructured bulk as a reference (Fig. 4b). In fact, SAXS data give information on the angular dependence of the diffused intensity of X-ray radiation of specific wavelength by the system. The scattered X-ray intensity in a specific direction is in turn dependent on size, shape, and density of the inhomogeneities responsible for the scattering process [49], analogously to optical diffusion of light by submicroscopic scatterers in transparent media.

The first step of the analysis transforms the experimental patterns in Fig. 4a, b in patterns reported in reciprocal scale (Fig. 4c, d) so as to extract sections of the scattering image as a function of the in-plane q_{xy} scattering vector and the out-of-plane q_z scattering vector at, respectively, $q_z \approx 0$ or $q_{xy} \approx 0$. Whilst the condition $q_{xy} \approx 0$ is determined by the orientation of the incidence plane (which divides the pattern in two symmetric fields in Fig. 4a), the origin of the q_z axis has been fixed at the bright streak corresponding to the Yoneda scattering peak – at the critical angle of total reflection – as an internal reference within the set of samples. In this way the SAXS patterns in Fig. 4e, f are obtained.

These data, in log-log scale, give a qualitative insight into the nanomorphological features on the different structural levels, both in-plane and out-of-plane. In the in-plane data in Fig. 4e (q_{xy} data), at least two distinct power law Porod's regions can be found with a negative exponent close to 4, as expected from smooth surfaces [49], or slightly less,

pointing to the formation of interphases with a more complex morphology. The first region (1_{xy} in Fig. 4e) at large-q values (on the shortest structural scale) lies between 0.3 and 0.4 nm^{-1}, in semi-quantitative agreement with the AFM evidence of a dispersion of small nucleated nanoparticles with size in the 10^1 nm range. The deviation from the −4 slope is consistent with the formation of a corrugated boundary of the single nanoparticle. The aggregation of small nanoparticles in larger aggregates – as highlighted by the observed thermally activated changes of nanostructure size dispersion in Fig. 3 – is in turn confirmed by the occurrence of a second region (2_{xy} in Fig. 4e) at small-q values, between 0.1 and 0.2 nm^{-1}. In this region, the slope is close to −4, suggesting that on this structural level the nanoaggregation of nanoparticles gives rise to a quite stepwise and smooth boundary, as in fact observed in AFM. The deviation from Porod's law at q values smaller than 0.1 nm^{-1} suggests correlation effects at the length scale of 10^2 nm, consistently with the occurrence of nanoaggregates a few 10^2 nm in size. By contrast, the out-of-plane data show one Porod's region (1_z in Fig. 4e) which falls at larger q values, between 0.8 and 1.0 nm^{-1}, with a slope slightly deviating from −4. Large deviations from Porod's behaviour towards an intermediary correlation region instead occur at q_z values of 0.6–0.8 nm^{-1}, according to correlation effects in the length range of few nm. This outcome points to the occurrence of very thin nanostructures, which is consistent with the observation of nanostructures even in films only a few nm thick, as observed in AFM images (Fig. 3e, f). The nanomorphology on this smaller structural level in out-of-plane data turns out quite similar to the result we find in bulk material (Fig. 4f). However, in the latter case, very similar behaviours are registered in plane and out-of-plane. In bulk, in fact, the data point to basically spheroidal nanostructures few nm in size, as assessed by previous studies [11], with a quite corrugate interphase signalled by clear deviation from the −4 slope.

In summary, SAXS data on thin films indeed account for the nanostructures observed in AFM images, with sizes ranging from 10^1 to 10^2 nm and quite sharp outlines. Importantly, the articulated SAXS results clarify that such nanostructures are almost two-dimensional aggregates with lenticular shape, made of smaller nanoparticles few nm in size, moderately larger in the xy plane than along the z-axis.

3.4. Nanostructure phase and crystalline domain

The data discussed so far highlight several morphological details on different length scales. However, from such data, no detailed
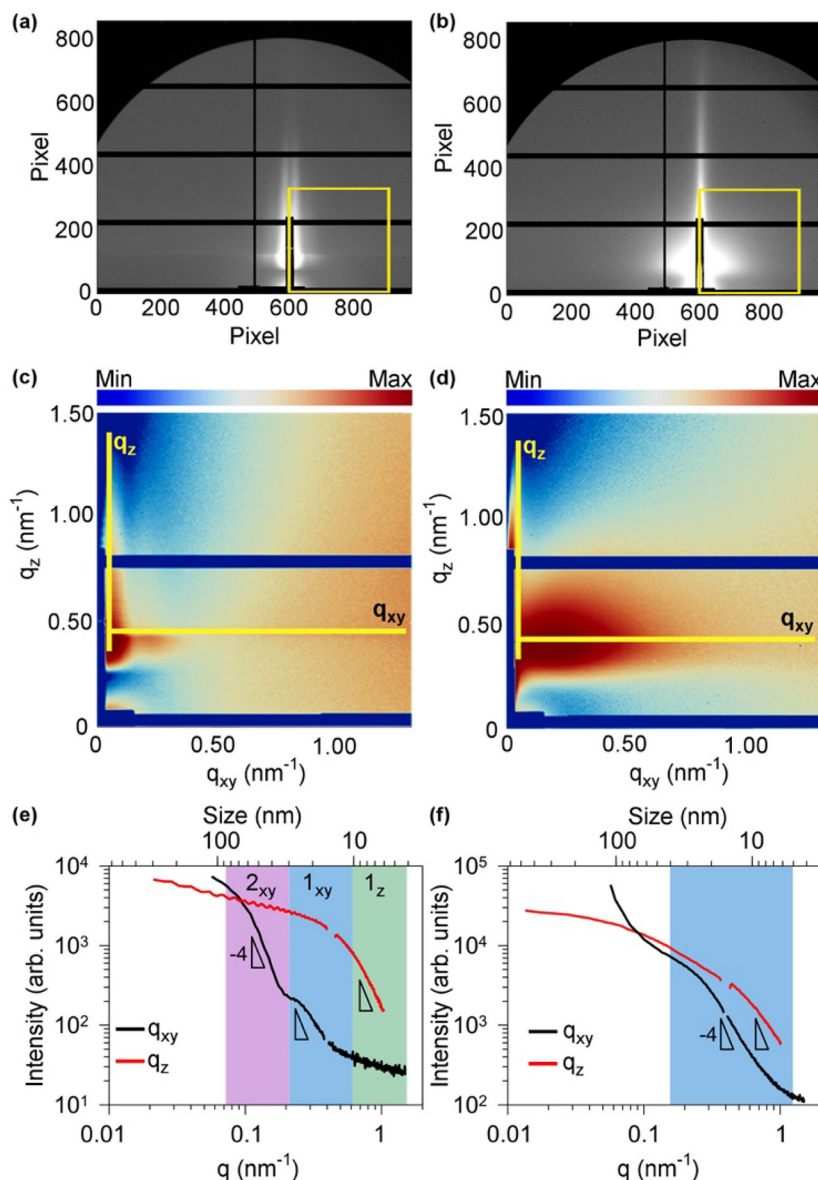
Fig. 4. Small Angle X-ray Scattering data. (a) and (b) Full angular field pattern of SAXS experiment on a 130 nm thick as-deposited film and, respectively, a bulk sample with the same composition and nanocrystallized by thermal treatment at 690 °C for 15 min. (c) and (d) SAXS patterns in scattering vector q-scale from the scattering regions indicated by squares in the experimental patterns (a) and (b), respectively; vertical and horizontal yellow stripes indicate the pattern regions used for the analysis of out-of-plane (vertical region along q_z) and in-plane scattered intensity (horizontal stripe along q_{xy}). (e) and (f) log-log representation of the intensity pattern sections indicated in (c) and (d) by the yellow regions as a function of q_{xy} and q_z scattering vectors. Triangles are drawn as a slope reference of the expected power dependence (with exponent − 4) in case of Porod's behaviour. Different structural levels in the SAXS response are highlighted by differently coloured regions. (For interpretation of the references to colour in this figure legend, the reader is referred to the web version of this article.)

information can be extracted about the phase of the observed nano-structures. The nanophase, in fact, could be ascribed either to composi-tional nano-inhomogeneity – caused for instance to phase separation between Ga-rich and Ga-poor amorphous oxides – or to Ga_2O_3 nanocrystals, as observed in bulk material, or to other unexpected compositions.

Information can be obtained on this final structural level from the analysis of XRD data. Fig. 5a reports XRD patterns collected on films treated at different temperature, while Fig. 5b and c show the effects of the different thickness and, respectively, of the duration of the ther-mal treatment. In all the patterns, just on the tail of the broad halo aris-ing from the amorphous silicate-based matrix [50], three reflections are registered at about 31°, 36° and 44°. This set of reflections is ascribable to a crystalline Ga-oxide spinel phase, such as γ-Ga_2O_3 or $LiGa_5O_8$,

according to the PDF files of the two compounds (γ-Ga_2O_3, ICDD PDF2 #00–020-0426, and Ga_5LiO_8, ICDD PDF2 #01–076-0199) [40,51].

Importantly, this result confirms the propensity of Ga-Si-Ge oxide system to undergo phase separation in thin planar geometry too, forming γ-Ga_2O_3 nanophases incorporated in germanosilicate amor-phous films. Indeed, the data show an even greater propensity to nano-phase separation than in bulk, with evidence of Ga-oxide spinel phase in films not necessarily thermally treated at or above 600 °C as instead required in bulk material. It is worth noting that the linewidth of these reflections, ranging between 2θ equal to 2° and 3°, is quite large and comparable to what has been observed in XRD patterns of Ga-oxide nanopowders [51–53]. The results of the linewidth analysis through Scherrer's law are reported in Fig. 5d, e and f in term of size of the crys-talline domain, together with the normalized intensity. It is worth noting
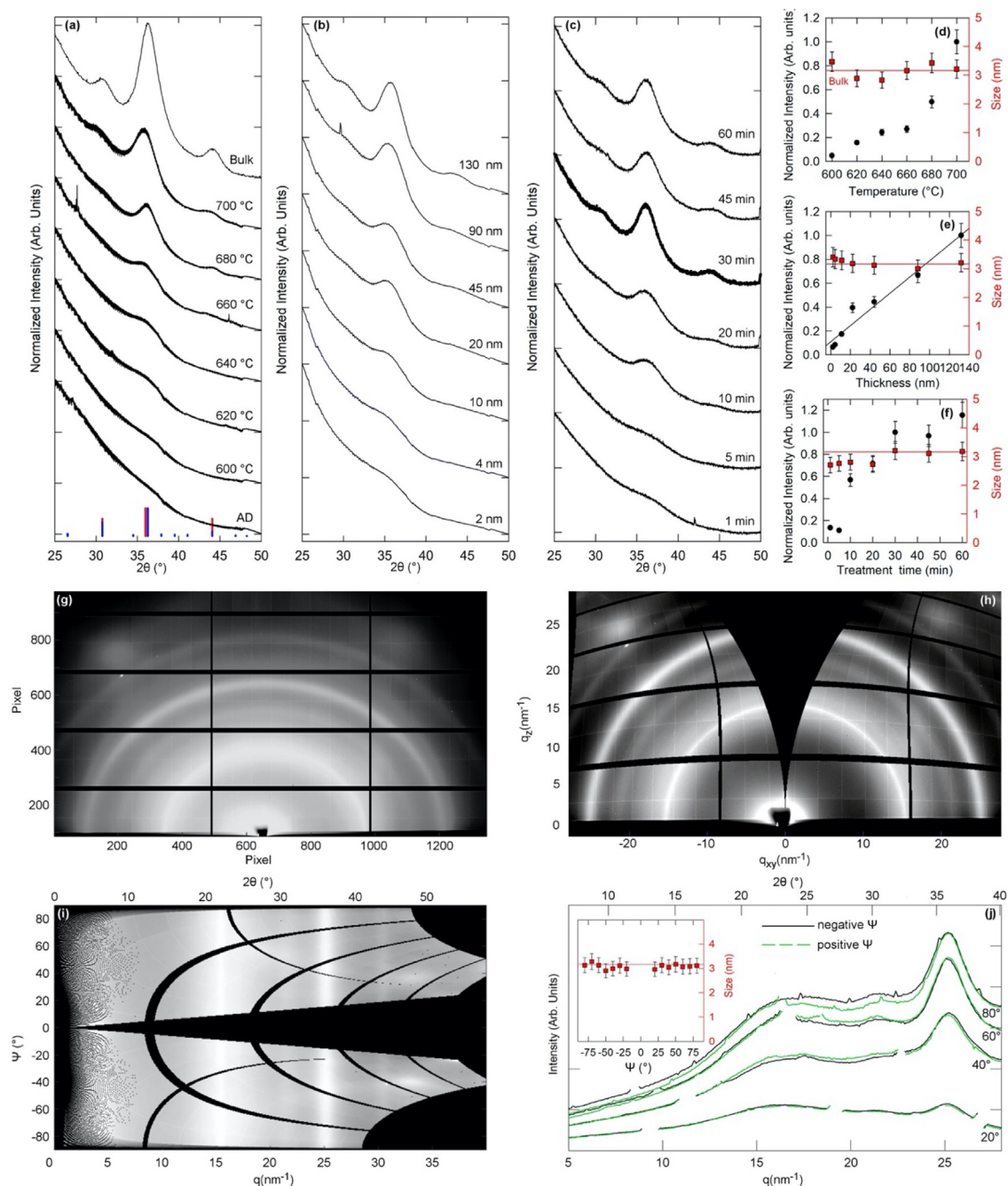
Fig. 5. XRD analysis. (a) XRD patterns of films (about 130 nm thick) treated at the indicated temperature for 30 min, compared with as-deposited film and a bulk sample nano-crystallized by thermal treatment at 690 °C for 15 min. Vertical lines indicate the positions of the main reflections of $LiGa_5O_8$ (blue) and γ-Ga_2O_3 (red). (b) XRD patterns of films with different thickness (from 2 nm to about 130 nm) treated at 700 °C for 30 min. (c) XRD patterns of films (about 130 nm thick) treated at 700 °C for different duration time from 1 min to 60 min. Patterns in (a), (b) and (c) are raw data after equal scaling in the reported range and vertically shifted for clarity. (d), (e) and (f) Dependence of the main reflection at about 36° on treatment temperature, film thickness, and treatment duration: (left axis, circles) XRD net peak area (corrected for acquisition time) normalized to the 130 nm thick sample treated at 700 °C for 30 min; (right axis, squares) crystalline domain size from Scherrer analysis (horizontal lines are drawn as a reference of the crystalline domain size in bulk, while the other straight line in (e) is a guide for the eye). (g) GI-XRD two-dimensional pattern of a representative sample (130 nm thick, treated at 700 °C for 30 min) in the real space. (h) GI-XRD data in (g) after transformation in q-representation. (i) GI-XRD data from (h) in the polar-space, with Ψ the out-of-plane polar angle. (j) One-dimensional XRD patterns obtained from sections of (i), after a minor correction for the background, at different negative (continuous black line) and positive (dashed green line) Ψ values, from 20° to 80° out-of-plane. Inset: crystalline size from Scherrer analysis vs. Ψ. (For interpretation of the references to colour in this figure legend, the reader is referred to the web version of this article.)

that the crystalline domain does not significantly change by modifying the conditions of the thermal treatments, with a mean value quite stable at around 3 nm. Only as-deposited films actually show broader patterns, which suggest smaller crystalline domains – although not reliably quantifiable – possibly affected by large structural disorder, as in Ga-oxide colloidal nanophases [54]. Interestingly, the mean value of crystalline size in all the films is consistent, within the experimental uncertainty, with the

minimum value of film thickness, and does not increase by increasing the thickness by up to about two order of magnitude. Therefore, the results do not show detectable evidence of spatial constraints to the crystal growth in planar geometry, but a self-limitation of crystal size at the used condition of film preparation.

Despite the lack of any appreciable change of crystalline domain size after thermal treatments and for different thickness values, the intensity

of the Ga-oxide pattern increases by increasing treatment temperature and duration time. This fact points to a thermally activated mechanism that enhances the amount of the separated phase through the continuous nucleation of Ga-oxide nanocrystals, but without a relevant process of nanocrystal growth. Therefore, the changes of nanoparticle size distribution we observe in AFM images after thermal treatments must be ascribed to a process of nanocrystals aggregation – accompanied by nanocrystal nucleation – with a negligible contribution of crystal growth.

Further details on a shorter structural level can be given through the analysis of two-dimensional GIXRD results. The starting experimental data in the real space, as in Fig. 5g, is converted in reciprocal coordinates (intensity in the q_{xy} - q_z plane, as in Fig. 5h) and then reported as a collection of diffraction patterns, in q scattering vector, as a function of the out-of-plane polar angle Ψ, as reported in Fig. 5i. In Fig. 5j, XRD spectra are extracted from Fig. 5i at different values of Ψ. Interestingly, the data do not register any relevant dependence on Ψ (inset in Fig. 5j), pointing to a substantial isotropy of the extent of the crystalline domain, quite independently of the shape anisotropy of the nanostructures at the higher structural levels.

3.5. Overall picture and role of planar geometry

All the pieces of information that has been collected so far on the different length scales within the full matrix of samples at different thickness and thermal treatment can now be joined together. The description of the material features can be sketched as they emerge from the different types of data concerning the overall morphology and the underlying substructure within the nanoparticles formed by segregation and aggregation mechanisms in the various processes of deposition and thermal treatment.

The deposition process gives rise to a fully densified non-porous material with density and composition close to the parent glass (XRR data) and equal to about 3.7×10^3 kg m^{-3}. At the same time – probably for the relevant kinetic energy of the matter impinging on the substrate – the deposition process brings the native segregation of a nanophase aggregated in form of nanoparticles in a matrix (AFM images). The nanoparticles have different size, the smallest ones being few nm in size in the film plane (AFM data), and 98% with lateral size below 100 nm. These nanoparticles are almost symmetric spheroids, slightly flattened in the direction normal to the film surface, with vertical size of the same order of magnitude of the minimum film thickness investigated (GIXRD data), about 8–10 nm in film 130 nm thick. The size of the smallest nanoparticles is consistent with the crystalline domain of the nanophase, which grows by thermal activation up to a maximum mean value of about 3 nm as spinel Ga-oxide phase (XRD). Both in as-deposited and in thermally treated films, the crystalline domain appears isotropic, in contrast with the variety of in-plane sizes of the nanostructures within the same sample and as a function of treatment and film thickness. In fact, a second structural level occurs (SAXS data) as nanoaggregates of small nanoparticles, with in-plane size ranging from few 10^1 nm to almost 1 μm (SAXS and AFM data). This structural level points to a process of formation and thermally activated growth of these aggregates which proceeds laterally along the film plane (AFM data). The aggregation process modifies the size distribution consistently with the occurrence of ripening or coalescence of small nanoparticles. This effect is relevant in thermal treated films, in which lateral aggregation gives rise to the increase of the fraction of nanostructures larger than 500 nm, changing from 0.4% to 0.6% by treating 30 min at 640 °C and then at 4.5% by treating at 700 °C. However, the results show that thermal treatments also promote the small nanoparticle nucleation, which increases with the temperature with a maximum yield at temperature comprised between the glass transition temperature and the crystallization temperature of the compound (AFM statistical data analysis). The strong anisotropy of the nanostructures –growing laterally much faster than normally to the film – points to a relevant

role of planar geometry as an effective constraint to the diffusion mechanism driving the aggregation of the nucleating phase, while an isotropic crystallization proceeds on the scale of only a few nm.

4. Conclusions

The present results – obtained from analyses on different structural scales, from XRR patterns to AFM images, from SAXS to GIXRD patterns – draw an articulated picture of how the sub-micrometre features of thin layers of Ga$_2$O$_3$-containing alkali germanosilicate turn out to be shaped and nanostructured as a result of the film deposition process and the thermal treatments. Importantly, the results show that sputtering techniques permit a prompt fabrication of thin films with native nanostructured features, without the need of post-synthesis treatments instead required for nano-crystallization of bulk material. The comparison with the results on bulk material points to further interesting peculiarities of the material produced in planar geometry. Specifically, thermal treatments of the deposited films mainly increase the mean lateral size of the nanostructures, keeping the vertical size smaller than or comparable with the film thickness. As a result, the data demonstrates that – in the investigated treatment temperature range between 600 and 700 °C – nanoparticle aggregation mechanisms successfully preserve a nanostructured topology comprising nano-systems fully surrounded by an amorphous dielectric matrix. This structural feature and the possibility of changing the mean distance between nanostructures by changing the nanostructure size distribution by thermal treatment give a tool for tailor the material according to desired charge transport mechanisms mediated by the nanostructures themselves. In summary, the outcome is a description that fills the gap of knowledge on the scalability of this compound to the planar geometry, giving also a valuable indication of the effective role of planar geometry and treatments on the nanostructuring process. Such achievements give the required basis for the exploitation of Ga-containing mixed oxides in planar technology.

Data availability

The data that support the findings of this study are available from the corresponding author upon reasonable request.

Declaration of Competing Interest

The authors declare that they have no known competing financial interests or personal relationships that could have appeared to influence the work reported in this paper.

Acknowledgements

References

[1] M. Vahak, Nano-Glass Ceramics: Processing, Properties and Applications, Elsevier, Amsterdam, 2015.

[2] J.A. Hollingsworth, V.I. Klimov, Semiconductor and Metals Nanocrystals, Marcel Dekker, New York, 2004.

[3] S.F. Zhou, C.Y. Li, G. Yang, G. Bi, B.B. Xu, Z.L. Hong, K. Miura, K. Hirao, J.R. Qiu, Self-limited Nanocrystallization-mediated activation of semiconductor Nanocrystal in an amorphous solid, Adv. Funct. Mater. 23 (43) (2013) 5436–5443.

[4] J. Del Castillo, V.D. Rodriguez, A.C. Yanes, J. Mendez-Ramos, M.E. Torres, Luminescent properties of transparent nanostructured Eu^{3+} doped SnO$_2$-SiO$_2$ glass-ceramics prepared by the sol-gel method, Nanotechnology 16 (5) (2005) S300–S303.

[5] A.C. Yanes, A. Santana-Alonso, J. Mendez-Ramos, J. Del-Castillo, V.D. Rodriguez, Novel sol-gel nano-glass-ceramics comprising Ln(3+)-Doped YF3 nanocrystals: structure and high efficient UV Up-conversion, Advanced Functional Materials 21 (16) (2011) 3136–3142.

[6] S. Chenu, E. Veron, C. Genevois, G. Matzen, T. Cardinal, A. Etienne, D. Massiot, M. Allix, Tuneable Nanostructuring of highly transparent zinc Gallogermanate glasses and glass-ceramics, Advanced Optical Materials 2 (4) (2014) 364–372.

[7] R.G. Fernandes, D.F. Franco, V.R. Mastelaro, T. Cardinal, O. Toulemonde, M. Nalin, Thermal and structural modification in transparent and magnetic germanoborate glasses induced by Gd2O3, Ceram. Int. 46 (14) (2020) 22079–22089.

[8] S.F. Zhou, N. Jiang, B.T. Wu, J.H. Hao, J.R. Qiu, Ligand-driven wavelength-tunable and ultra-broadband infrared luminescence in single-ion-doped transparent hybrid materials, Adv. Funct. Mater. 19 (13) (2009) 2081–2088.

[9] S. Brovelli, N. Chiodini, R. Lorenzi, A. Lauria, M. Romagnoli, A. Paleari, Fully inorganic oxide-in-oxide ultraviolet nanocrystal light emitting devices, Nature Communications 3 (2012).

[10] N.V. Golubev, E.S. Ignat'eva, V.M. Mashinsky, E.O. Kozlova, V.N. Sigaev, A. Monguzzi, A. Paleari, R. Lorenzi, Pre-crystallization heat treatment and infrared luminescence enhancement in Ni2+-doped transparent glass-ceramics, J. Non-Cryst. Solids 515 (2019) 42–49.

[11] V.N. Sigaev, N.V. Golubev, E.S. Ignat'eva, B. Champagnon, D. Vouagner, E. Nardou, R. Lorenzi, A. Paleari, Native amorphous nanoheterogeneity in gallium germanosilicates as a tool for driving Ga2O3 nanocrystal formation in glass for optical devices, Nanoscale 5 (2013) 299–306.

[12] V.N. Sigaev, N.V. Golubev, E.S. Ignat'eva, A. Paleari, R. Lorenzi, Light-emitting Ga-oxide nanocrystals in glass: a new paradigm for low-cost and robust UV-to-visible solar-blind converters and UV emitterst, Nanoscale 6 (3) (2014) 1763–1774.

[13] A. Paleari, N.V. Golubev, E.S. Ignat'eva, V.N. Sigaev, R. Lorenzi, Donor-acceptor control in grown-in-glass gallium oxide Nanocrystals by crystallization-driven Heterovalent doping, Chemphyschem 18 (6) (2017) 662–669.

[14] N.V. Golubev, E.S. Ignat'eva, V.N. Sigaev, L. De Trizio, A. Azarbod, A. Paleari, R. Lorenzi, Nucleation-controlled vacancy formation in light-emitting wide-band-gap oxide nanocrystals in glass, J. Mater. Chem. C 3 (17) (2015) 4380–4387.

[15] B. Wu, S. Zhou, J. Ren, D. Chen, X. Jiang, C. Zhu, J. Qiu, Broadband infrared luminescence from transparent glass-ceramics containing Ni2+-doped beta- Ga2O3 nanocrystals, Applied Physics B-Lasers and Optics 87 (4) (2007) 697–699.

[16] S.F. Zhou, H.F. Dong, G.F. Feng, B.T. Wu, H.P. Zeng, J.R. Qiu, Broadband optical amplification in silicate glass-ceramic containing beta- Ga2O3: Ni2+ nanocrystals, Opt. Express 15 (9) (2007) 5477–5481.

[17] S.F. Zhou, G.F. Feng, B.T. Wu, N. Jiang, S.Q. Xu, J.R. Qiu, Intense infrared luminescence in transparent glass-ceramics containing beta- Ga2O3 : Ni2+ nanocrystals, J. Phys. Chem. C 111 (20) (2007) 7335–7338.

[18] S.Q. Xu, D.G. Deng, R.Q. Bao, H.D. Ju, S.L. Zhao, H.P. Wang, B.L. Wang, Ni2+-doped new silicate glass-ceramics for superbroadband optical amplification, Journal of the Optical Society of America B-Optical Physics 25 (9) (2008) 1548–1552.

[19] Z.G. Gao, X.S. Lu, Y.S. Chu, S. Guo, L. Liu, Y.Y. Liu, S.Y. Sun, J. Ren, J. Yang, The distribution of rare earth ions in a gamma- Ga2O3 nanocrystal-silicate glass composite and its influence on the photoluminescence properties, J. Mater. Chem. C 6 (12) (2018) 2944–2950.

[20] W.K. Bae, J. Kwak, J. Lim, D. Lee, M.K. Nam, K. Char, C. Lee, S. Lee, Multicolored light-emitting diodes based on all-quantum-dot multilayer films using layer-by-layer assembly method, Nano Lett. 10 (7) (2010) 2368–2373.

[21] J.S. Bendall, M. Paderi, F. Ghigliotti, N.L. Pira, V. Lambertini, V. Lesnyak, N. Gaponik, G. Visimberga, A. Eychmuller, C.M.S. Torres, M.E. Welland, C. Gieck, L. Marchese, Layer-by-layer all-inorganic quantum-dot-based LEDs: a simple procedure with robust performance, Adv. Funct. Mater. 20 (19) (2010) 3298–3302.

[22] A. Paleari, S. Brovelli, R. Lorenzi, M. Giussani, A. Lauria, N. Mochenova, N. Chiodini, Tunable dielectric function in electric-responsive glass with tree-like percolating pathways of chargeable conductive nanoparticles, Adv. Funct. Mater. 20 (20) (2010) 3511–3518.

[23] J. Remondina, A. Paleari, N.V. Golubev, E.S. Ignat'eva, V.N. Sigaev, M. Acciarri, S. Trabattoni, A. Sassella, R. Lorenzi, Responsive charge transport in wide-band-gap oxide films of nanostructured amorphous alkali-gallium-germanosilicate, J. Mater. Chem. C 7 (25) (2019) 7768–7778.

[24] Hyun-Gyu Hwang, Jong-Un Woo, Tae-Ho Lee, Sung-Mean Park, Tae-Gon Lee, Woong-Hee Lee, Sahn Nahm, Synaptic plasticity and preliminary-spike-enhanced plasticity in a CMOS-compatible Ta2O5 memristor, Mater Design 187 (2020) 108400.

[25] Yu Yu Zhiliang Chen, Lufan Jin, Yifan Li, Qingyan Li, Tengteng Li, Yating Zhang, Haitao Dai, Jianquan Yao, Artificial synapses with photoelectric plasticity and memory behaviors based on charge trapping memristive system, Mater Design 188 (2020) 108415.

[26] A.C. Khot, N.D. Desai, K.V. Khot, M.M. Salunkhe, M.A. Chougule, T.M. Bhave, R.K. Kamat, K.P. Musselman, T.D. Dongale, Bipolar resistive switching and memristive properties of hydrothermally synthesized TiO2 nanorod array: effect of growth temperature, Mater Design 151 (2018) 37–47.

[27] Qu Bo, Du Haiwei, Tao wan, xi Lin, Adnan Younis, Dewei Chu, synaptic plasticity and learning behavior in transparent tungsten oxide-based memristors, Mater Design 129 (2017) 173–179.

[28] Jun Ge, Haiming Huang, Zelin Ma, Weilong Chen, Xucheng Cao, Huaheng Fang, Jianfeng Yan, Zhiyu Liu, Weiliang Wang, Shusheng Pan, A sub-500 mV monolayer hexagonal boron nitride based memory device, Mater Design 198 (2021) 109366.

[29] A.A. Gismatulin, V.A. Voronkovskii, G.N. Kamaev, Y.N. Novikov, V.N. Kruchinin, G.K. Krivyakin, V.A. Gritsenko, I.P. Prosvirin, A. Chin, Electronic structure and charge transport mechanism in a forming-free SiOx-based memristor, Nanotechnology 31 (2020) 505704.

[30] Jun-Hwe Cha, Sang Yoon Yang, Jungyeop Oh, Shinhyun Choi, Sangsu Park, Byung Chul Jang, Wonbae Ahna, Sung-Yool Choi, Conductive-bridging random-access memories for emerging neuromorphic computing, Nanoscale 12 (2020) 14339–14368.

[31] M. Talaeizadeh, L. Jamilpanah, S.A. Seyed Ebrahimi, S.M. Mohseni, Resistive switching characteristics of Co2FeSi and Mn with Al2O3 granular nanocomposites, J. Magn. Magn. Mater. 516 (2020) 167336.

[32] Wen Zhou, Rui Yang, Hui-Kai He, He-Ming Huang, Jue Xiong, Xin Guo, Optically modulated electric synapses realized with memristors based on ZnO nanorods, Appl. Phys. Lett. 113 (2018) 061107/1–5.

[33] Karl Berggren, et al., Roadmap on emerging hardware and technology for machine learning, Nanotechnology 32 (2020), 012002, .

[34] J.A. Thornton, Influence of apparatus geometry and deposition conditions on the structure and topography of thick sputtered coatings, J. Vac. Sci. Technol. 11 (1974) 666–670.

[35] J.A. Thornton, The microstructure of sputter-deposited coatings, J. Vac. Sci. Technol. A 4 (1986) 3059–3065.

[36] I. Petrov, P.B. Barna, L. Hultman, J.E. Greene, Microstructural evolution during film growth, J. Vac. Sci. Technol. A 21 (2003) S117–S128.

[37] J.E. Greene, Review article: tracing the recorded history of thin-film sputter deposition: From the 1800s to 2017, J. Vac. Sci. Technol. A 35 (2017) 05C204/1–60.

[38] S.M. Danauskas, D.X. Li, M. Meron, B.H. Lin, K.Y.C. Lee, Stochastic fitting of specular X-ray reflectivity data using StochFit, J. Appl. Crystallogr. 41 (2008) 1187–1193.

[39] B. Schrode, S. Pachmajer, M. Dohr, C. Rothel, J. Domke, T. Fritz, R. Resel, O. Werzer, GIDVis: a comprehensive software tool for geometry-independent grazing-incidence X-ray diffraction data analysis and pole-figure calculations, J. Appl. Crystallography 52 (2019) 683–689.

[40] N.V. Golubev, E.S. Ignat'eva, V.N. Sigaev, A. Lauria, L. De Trizio, A. Azarbod, A. Paleari, R. Lorenzi, Diffusion-driven and size-dependent phase changes of gallium oxide nanocrystals in a glassy host, Phys. Chem. Chem. Phys. 17 (7) (2015) 5141–5150.

[41] E. Chason, T.M. Mayer, Thin film and surface characterization by specular X-ray reflectivity, Critical Reviews in Solid State and Materials Sciences 22 (1) (1997) 1–67.

[42] P. Lenormand, A. Lecomte, D. Babonneau, A. Dauger, X-ray reflectivity, diffraction and grazing incidence small angle X-ray scattering as complementary methods in the microstructural study of sol–gel zirconia thin films, Thin Solid Films 495 (2006) 224–231.

[43] F. Lo Celso, A. Triolo, F. Negroni, M. Hainbuchner, M. Baron, P. Strunz, H. Rauch, R. Triolo, Structural investigation of hybrid nanocomposites, Appl. Phys. A Mater. Sci. Process. 74 (2002) S1430–S1432.

[44] C.M. Sorensen, W.B. Hageman, Two-dimensional soot, Langmuir 17 (18) (2001) 5431–5434.

[45] N. Severin, I.M. Sokolov, J.P. Rabe, Dynamics of ethanol and water mixtures observed in a self-adjusting molecularly thin slit pore, Langmuir 30 (12) (2014) 3455–3459.

[46] C. Haley, J.H. Weaver, Buffer-layer-assisted nanostructure growth via two-dimensional cluster-cluster aggregation, Surf. Sci. 518 (3) (2002) 243–250.

[47] S. Lenz, M. Bonini, S.K. Nett, M.C. Lechmann, S.G.J. Emmerling, R.S. Kappes, M. Memesa, A. Timmann, S.V. Roth, J.S. Gutmann, Global scattering functions: a tool for grazing incidence small angle X-ray scattering (GISAXS) data analysis of low correlated lateral structures, European Physical Journal-Applied Physics 51 (1) (2010).

[48] T.P. Rieker, S. Misono, F. Ehrburger-Dolle, Small-angle X-ray scattering from carbon blacks: crossover between the fractal and Porod regimes, Langmuir 15 (4) (1999) 914–917.

[49] P.W. Schmidt, Small-angle scattering studies of disordered, porous and fractal systems, J. Appl. Crystallogr. 24 (1991) 414–435.

[50] A. Hamoudi, L. Khouchaf, C. Depecker, B. Revel, L. Montagne, P. Cordier, Microstructural evolution of amorphous silica following alkali-silica reaction, J. Non-Cryst. Solids 354 (45–46) (2008) 5074–5078.

[51] T. Wang, S.S. Farvid, M. Abulikemu, P.V. Radovanovic, Size-tunable phosphorescence in colloidal metastable gamma- Ga2O3 Nanocrystals, J. Am. Chem. Soc. 132 (27) (2010) 9250–9252.

[52] N. Pinna, G. Garnweitner, M. Antonietti, M. Niederberger, A general nonaqueous route to binary metal oxide nanocrystals involving a C-C bond cleavage, J. Am. Chem. Soc. 127 (15) (2005) 5608–5612.

[53] R. Lorenzi, A. Paleari, N.V. Golubev, E.S. Ignat'eva, V.N. Sigaev, M. Niederberger, A. Lauria, Non-aqueous sol-gel synthesis of hybrid rare-earth-doped gamma-Ga2O3 nanoparticles with multiple organic-inorganic-ionic light-emission features, J. Mater. Chem. C 3 (2015) 41–45.

[54] H.Y. Playford, A.C. Hannon, M.G. Tucker, D.M. Dawson, S.E. Ashbrook, R.J. Kastiban, J. Sloan, R.I. Walton, Characterization of structural disorder in gamma-Ga2O3, J. Phys. Chem. C 118 (29) (2014) 16188–16198.